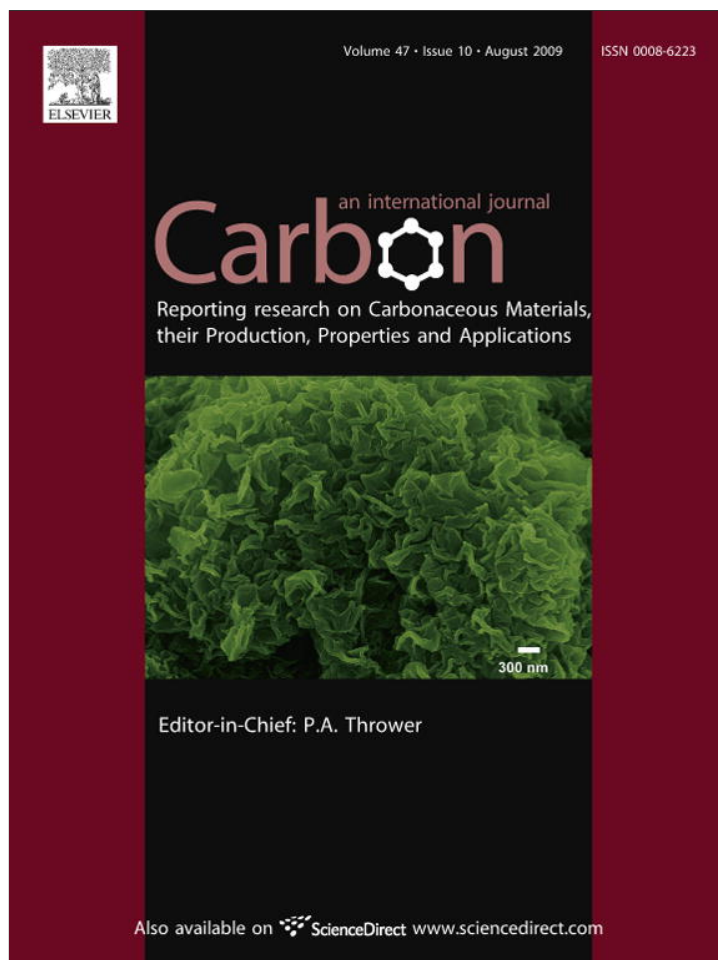


Provided for non-commercial research and education use.
Not for reproduction, distribution or commercial use.



This article appeared in a journal published by Elsevier. The attached copy is furnished to the author for internal non-commercial research and education use, including for instruction at the authors institution and sharing with colleagues.

Other uses, including reproduction and distribution, or selling or licensing copies, or posting to personal, institutional or third party websites are prohibited.

In most cases authors are permitted to post their version of the article (e.g. in Word or Tex form) to their personal website or institutional repository. Authors requiring further information regarding Elsevier's archiving and manuscript policies are encouraged to visit:

<http://www.elsevier.com/copyright>

available at www.sciencedirect.comjournal homepage: www.elsevier.com/locate/carbon

Resonant Raman spectra of graphene with point defects

Valentin N. Popov*, Luc Henrard, Philippe Lambin

Research Center in Physics of Matter and Radiation, Facultés Universitaires Notre Dame de la Paix, Namur B-5000, Belgium

ARTICLE INFO

Article history:

Received 22 October 2008

Accepted 27 April 2009

Available online 7 May 2009

ABSTRACT

The Raman spectra of graphene with three different types of point defects, namely, a mono-vacancy, a di-vacancy, and a Stone–Wales defect, was calculated within a non-orthogonal tight-binding model using supercells of graphene with a single defect. The defects were found to modify the electronic structure and the phonons of graphene giving rise to new optical transitions and defect-related phonons. Based on the calculated Raman spectra, we determined the Raman lines that can serve as signatures of the specific defects. The comparison of the calculated Raman intensity of the graphitic (G-) band of perfect graphene and graphene with defects shows that the intensity can be enhanced up to one order of magnitude by the presence of defects.

© 2009 Elsevier Ltd. All rights reserved.

1. Introduction

Recent progress in production of a few-layer graphite [1] and the prospects for future application in nanoelectronics have put the single-layer graphite (so-called graphene) in the focus of many theoretical and experimental studies [2]. Point defects of type vacancy and topological defects can change the electronic and the vibrational properties of graphite, and therefore can modify its transport properties. Vacancies are formed in low concentrations [3] in graphite during defective growth. However, they are present in much larger quantities in irradiated materials or chemically treated ones and are the predominant defects in such materials [4]. Vacancies can be observed by high-resolution transmission electron microscopy (TEM) because they cause local deformation of the graphite surface [5]. The possible existence of a five-to-seven ring defect was suggested in 1969 [6]. A pair of adjacent five-to-seven ring defects can form a topological defect in graphene called the Stone–Wales (SW) defect [7]. This defect plays an important role in growth and annealing down to a structurally ordered state of carbon systems. Once formed, the SW defect can move along the structure, creating dislocations, and leading to large-scale structural rearrangements in graphitic networks [8]. The direct experimental identification

of SW defects by TEM is uncertain because they are usually present in small quantities and do not produce visible deformation of the graphite surface. A more reliable method for detection of point defects is based on the vibrational density of states derived by inelastic electron tunneling spectroscopy (IETS–STM) [9,10] and theoretical predictions [11].

A powerful and straightforward technique to study defects in carbon systems is the Raman spectroscopy. The Raman spectra of carbonaceous materials with sp^2 -hybridized regions exhibit a prominent defect-induced band at $\approx 1360\text{ cm}^{-1}$, so-called D-band, with position dependent on the laser excitation energy and intensity dependent on the relative content of these regions [12,13]. The Raman spectra of graphite with defects also show a few Raman lines, which can be ascribed to defect-assisted light scattering, the most intense being the D-band [14]. In a few-layer graphite, the D-band was found to depend on the number of layers [15] and on the doping [16]. These studies do not determine the type of the defects and at present there are no experimental observations and assignment of Raman features to specific types of defects. While it is difficult to study experimentally defects in graphene, some progress has been made in the theoretical study of the Raman signatures of defects. A bond-polarizability model has been used to derive the Raman intensity of the

* Corresponding author. Address: Faculty of Physics, University of Sofia, BG-1164 Sofia, Bulgaria.

E-mail address: vpopov@phys.uni-sofia.bg (V.N. Popov).

0008-6223/\$ - see front matter © 2009 Elsevier Ltd. All rights reserved.

doi:10.1016/j.carbon.2009.04.043

phonons of graphene with defects [17]. Recently, the non-resonant Raman spectra of such structures have been calculated within a first-principles approach using a single \mathbf{k} -point [18]. In this case, the computational approach has not allowed to handle large enough supercells, which could result in spurious phonons and incorrect Raman intensity.

In this paper, we use a density-functional-theory-based non-orthogonal tight-binding model [19,20] to obtain the phonons and their Raman excitation profiles for graphene with three types of point defects. In these three cases, we simulate the Raman spectra and discuss the Raman lines, which are associated with the defects and can be adopted as their signatures.

2. Theoretical background

The electronic band structure of graphene with a single point defect was calculated within a density-functional-theory-based non-orthogonal tight-binding (NOTB) model with four valence electrons per carbon atom [19,20]. The defect removes the two-dimensional periodicity of the graphene lattice and the calculations have to be accomplished for the entire lattice. In order to avoid this and to take advantage of the methods for periodic lattices, one can consider again a two-dimensional periodic structure but with a supercell, consisting of N two-atom unit cells of perfect graphene and containing a single point defect. The supercell has to be large enough to ensure negligible interaction between the defects of different supercells. In the NOTB model, the electronic problem is reduced to the following matrix eigenvalue equation

$$\sum_{r'} (H_{kr'r'} - E_k S_{kr'r'}) c_{kr'} = 0. \quad (1)$$

Here \mathbf{k} is the two-dimensional wavevector and the index r labels the valence orbitals of the supercell, $r = 1, 2, \dots, 8N$. The quantities $H_{kr'r'}$ and $S_{kr'r'}$ are given by the expressions

$$H_{kr'r'} = \sum_{\mathbf{l}} e^{i\mathbf{k}\cdot\mathbf{R}(\mathbf{l})} H_{rr'}(\mathbf{R}(\mathbf{l})) \quad (2)$$

and

$$S_{kr'r'} = \sum_{\mathbf{l}} e^{i\mathbf{k}\cdot\mathbf{R}(\mathbf{l})} S_{rr'}(\mathbf{R}(\mathbf{l})), \quad (3)$$

where $H_{rr'}$ and $S_{rr'}$ are the matrix elements of the Hamiltonian and the overlap matrix elements, respectively, between orbitals r and r' centered at two atoms in supercells connected by a lattice vector $\mathbf{R}(\mathbf{l})$; E_k is the one-electron eigenenergy and c_{kr} are the coefficients in the expansion of the one-electron wavefunction as a linear combination of the atomic orbitals of the supercell. We denote the solutions to the eigenvalue equation Eq. (1) as E_{km} , $m = 1, 2, \dots, 8N$.

For performing structural optimization one needs the total energy of the system and the forces acting on the atoms. In the NOTB model, it is given by the expression

$$E = \sum_{km}^{\text{occ}} E_{km} + \frac{1}{2} \sum_{ij(i \neq j)} \varphi(r_{ij}), \quad (4)$$

where the first term is the band energy E_{BS} (the summation is over all occupied states) and the second term is the repulsive energy E_{rep} , expressed as the sum of repulsive pair potentials φ between pairs of neighbors. The band contribution to the

forces on the atoms is given by the Hellmann–Feynman theorem. The repulsive contribution to the force is equal to the first derivative of the total repulsive energy with respect to the atomic position vector.

The zone-center phonons were calculated using a perturbative approach within the NOTB [21]. In this approach, the response of the electrons to the atomic displacements is described in the linear response approximation. It has the advantage over the frozen-phonon approach that it avoids computationally expensive enlarging of the original supercell in the calculation of forces on atoms and that it further allows one to derive the dynamical matrix in a single step. The dynamical matrix is obtained from the change of the total energy due to a static lattice deformation (a phonon) with a two-dimensional wavevector

$$\mathbf{u}(\mathbf{l}\kappa) = \mathbf{e}(\kappa\mathbf{q}) e^{i\mathbf{q}\cdot\mathbf{R}(\mathbf{l})} + c.c. \quad (5)$$

Here the index κ labels the atoms in the supercell, $\kappa = 1, 2, \dots, 2N$. The band contribution to the energy change is derived in second-order perturbation theory as a second-order polynomial in $\mathbf{u}(\mathbf{l}\kappa)$. The repulsive energy is expanded in series of $\mathbf{u}(\mathbf{l}\kappa)$ up to second order. The dynamical matrix is then obtained from the expression

$$D_{\alpha\beta}(\kappa\kappa'\mathbf{q}) = \frac{1}{m_c} \frac{\partial^2 (E_{BS} + E_{rep})}{e_{\alpha}(\kappa\mathbf{q}) e_{\beta}(\kappa'\mathbf{q})}, \quad (6)$$

where m_c is the mass of the carbon atom. The phonon eigenvalues and eigenvectors are then found as solutions to the phonon equations of motion.

We adopted the quantum-mechanical description of the Raman scattering process, in which the system of the electrons and the phonons of the system, and photons of the electromagnetic radiation, and their interactions are considered [22]. Restricting ourselves to Stokes processes, we retained only the terms of the Raman tensor, which give predominant contribution to the intensity. These processes include (a) absorption of a photon (energy E_L and polarization vector $\boldsymbol{\varepsilon}_L$) with excitation of the electronic subsystem from the ground state and creation of an electron–hole pair, (b) scattering of the electron (hole) by a phonon (frequency ω and polarization vector \mathbf{e}), and (c) annihilation of the electron–hole pair with emission of a photon (energy $E_S = E_L - \hbar\omega$ and polarization vector $\boldsymbol{\varepsilon}_S$) and return of the electronic subsystem to the ground state. The contribution of these processes to the Raman intensity is given by the expression [23]

$$I(E_L, \omega) = A \left| \sum \frac{p^S D p^{L*}}{(E_L - E - i\gamma_e)(E_S - E - i\gamma_e)} \right|^2. \quad (7)$$

Here, the quantity A is slightly dependent on E_L and temperature. The summation is over all pairs of vertical states $\mathbf{k}m$ and $\mathbf{k}m'$ of the valence band and the conduction band, respectively. E is the separation between two such states and γ_e is the excited state width. $p^{L,S}$ is the matrix element between two such states of the component of the momentum in the direction of the polarization vector $\boldsymbol{\varepsilon}_{L,S}$ and D is the electron–phonon coupling matrix element. The latter is determined by the scalar product of the derivative of E with respect to the atomic displacement vector $\mathbf{u}(\mathbf{l}\kappa)$ and the phonon eigenvector

$$D = \sqrt{\frac{\hbar}{2m_c\omega}} \sum_{i\gamma} e_{i\gamma} \frac{\partial E}{\partial u_{i\gamma}}. \quad (8)$$

Here, $u_{i\gamma}$ is the γ -component of the displacement of the i th atom of the supercell.

The electron–phonon coupling matrix element D depends essentially on the particular Raman-active mode eigenvector and the derivative of E with respect to the atomic displacement vector [23]. Similar derivative but for the general case of states $\mathbf{k}m$ and $\mathbf{k}'m'$ enters the expression of the dynamical matrix, Eq. (6) (see [21]). Compared to the ab initio phonon dispersion of graphene, the calculated one within our tight-binding model predicts accurately the low-frequency phonon branches but overestimates the high-frequency ones by up to 12.5% [21]. Because the dynamical matrix depends linearly on the electron–phonon matrix element and yields the squared phonon eigenfrequencies, we can conclude that for the high-frequency branches our matrix element is larger than the ab initio ones [24] roughly by 27%. Our model gives a fair description of the Kohn anomaly of the phonon dispersion of graphene in good agreement with the ab initio results [24].

3. Results and discussion

We considered three types of point defects: a Stone–Wales defect (SW), a mono-vacancy defect (MV), and a di-vacancy defect (DV), shown in Fig. 1a–c. We chose a supercell of size 5×5 primitive cells of perfect graphene and containing a single defect. The large size of the supercell ensures negligible interaction between the defects of different supercells. The atomic structure optimization was performed with a 5×5 Monkhorst–Pack mesh of \mathbf{k} -points. It was carried out until the residual forces on all atoms decreased below $0.01 \text{ eV}/\text{\AA}$. The angle between the primitive translation vectors of the superstructure remained close to 60° and therefore the deformations of the supercell due to the defect do not extend beyond its boundaries. The primitive translations were relaxed from 12.30 \AA for perfect graphene to 12.24 \AA (MV), 12.17 \AA (DV), and 12.34 \AA (SW). Largest changes of the atomic positions with respect to perfect graphene are present for atoms close to the defects (see Fig. 1a–c). The three atoms, closest to the vacancy in the MV structure, changed their relative separations to (1) 2.354 \AA and (2) twice 2.729 \AA , suggesting the formation of a weak covalent bond between two of them and leaving the third one unpaired. These values are

larger than the ab initio one of (1) 2.02 \AA (Ref. [11]), 2.10 \AA (Ref. [25]), and (2) 2.505 \AA (Ref. [11]). As a whole, the supercell remained almost flat after optimization (see also Ref. [18]), the only exclusion being the unpaired atom of the MV structure, which was displaced out of the graphene plane by 0.49 \AA . This displacement is close to the ab initio ones of 0.47 \AA (Ref. [25]) and 0.43 \AA (Ref. [11]) but is larger than the value of 0.18 \AA of spin-polarized calculations [26]. The separation of the two neighboring atoms of each of the two vacancies in the DV supercell reduces to 1.945 \AA , which is larger than the ab initio result of 1.71 \AA (Ref. [11]). The decrease of the separation between pairs of atoms in the DV structure suggests reaching stability through formation of weak covalent bonding between these atoms accompanied by disappearance of the dangling bonds.

Perfect graphene is a zero-gap semiconductor. Its band structure (not shown) has two linear bands crossing at the Fermi energy at the K-point of the Brillouin zone. The presence of a defect removes the degeneracy of the bands at the Fermi energy and opens a non-zero band gap. The computed electronic band structure of the three superstructures (see Fig. 2a–c) shows that they are semiconductors with gaps of $\approx 0.49 \text{ eV}$ (MV), $\approx 0.75 \text{ eV}$ (DV), and $\approx 0.21 \text{ eV}$ (SW). In the case of the MV defect, there are two localized bands close to the Fermi energy, due to the defect. The obtained band structures are in fair agreement with available ab initio ones [11].

The Raman spectrum of graphite is dominated by a strong line (so-called G-line) at $\approx 1582 \text{ cm}^{-1}$. It is due to the in-plane bond-stretching phonon called the G-mode. In perfect graphene this phonon is also Raman-active and is predicted at $\approx 1585 \text{ cm}^{-1}$. The results of the phonon calculations for perfect graphene within the present tight-binding model were reported elsewhere [21]. We note that this model yields the frequency of the G-mode at 1780 cm^{-1} , which is overestimating the experimental value by $\approx 12.5\%$. This is generally the case for phonons with predominantly bond-stretching character obtained within tight-binding models [17]. The calculations of the phonons of graphene with defects exhibit a large number of Raman-active phonons. They will be discussed further on in connection with their Raman intensity and their importance as spectroscopic signatures of the specific type of defect.

The Raman intensity of the G-mode of perfect graphene was calculated with a dense 50×50 Monkhorst–Pack mesh of \mathbf{k} -points necessary for achieving convergence of the sum

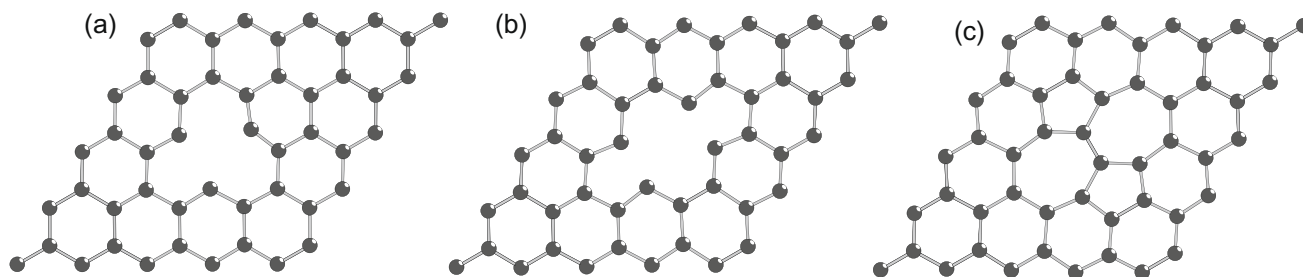


Fig. 1 – The optimized atomic structure of graphene with three different point defects: (a) a mono-vacancy (MV) defect, (b) a di-vacancy (DV) defect, and (c) a Stone–Wales (SW) defect. All three structures are almost flat except for the MV one, where the unpaired atom has a large out-of-plane displacement of 0.49 \AA .

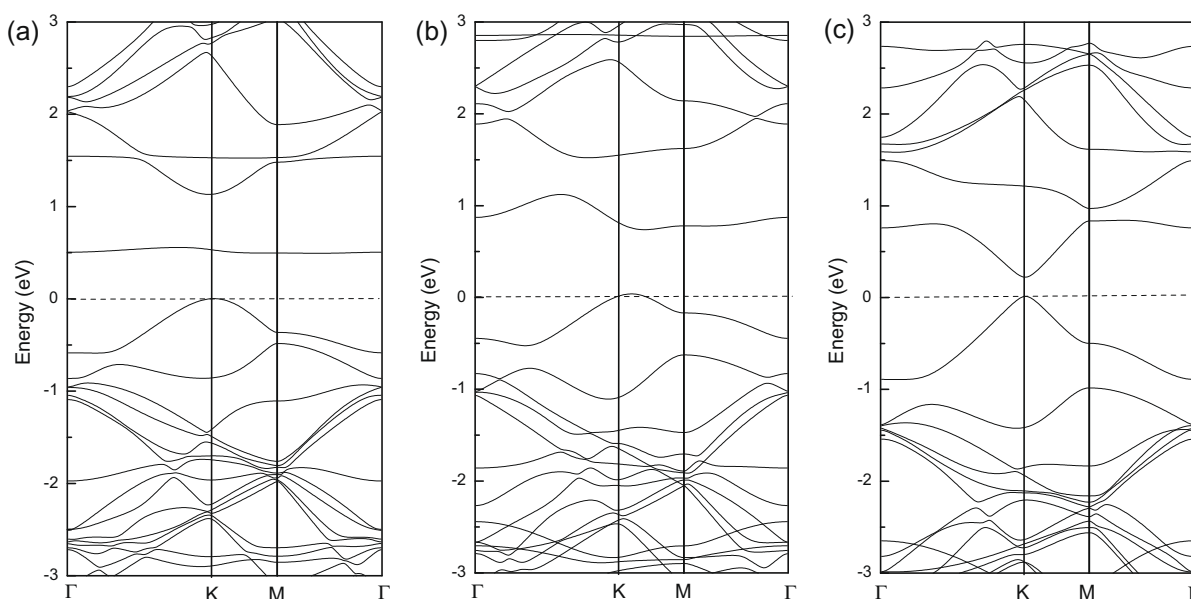


Fig. 2 – The electronic band structure of graphene with different point defects: (a) MV, (b) DV, and (c) SW. All three structures are semiconducting with gaps below 0.75 eV.

Eq. (7). The Raman experiments are normally performed on polycrystalline graphite samples with more or less random orientation of the micro-crystallites. Therefore, for comparison with future experimental data, we averaged the intensity over all spatial orientations of the light polarization, restricting ourselves to parallel scattering geometry. The obtained resonance excitation profile of the G-mode of perfect graphene, shown in Fig. 3a–c, increases monotonically with the increase of the photon energy in the visible range, in accord with experimental measurements on highly-oriented pyrolytic graphite (HOPG) [27].

The Raman intensity of graphene with defects was calculated for all Raman-active phonons and for all scattering geometries using a 30×30 Monkhorst–Pack mesh. The obtained resonance excitation profiles for the MV, DV, and SW cases (see Fig. 3a–c) exhibit resonant enhancement of the intensity close to optical transitions of graphene with defects. It is clear that this happens at laser photon energies, which are different for the three cases because of their different electronic structures. It is seen in the MV case that resonant

enhancement is present for all energies, in the DV case resonant scattering is possible for energies larger than about 2.2 eV, while for the SW case this is only possible for energies smaller than 2.5 eV. This observation can help in the assignment of the lines in the spectra of graphene with defects.

The obtained phonons and resonant excitation profiles were used to simulate the Raman spectra of graphene with the three types of defects for five commonly used laser photon energies: 1.96, 2.28, 2.41, 2.54, and 2.71 eV. It is clearly seen in Fig. 4a–c that Raman lines are present mainly up to $\approx 1000 \text{ cm}^{-1}$ (MV) and above $\approx 1000 \text{ cm}^{-1}$ (DV and SW). In these frequency ranges, the spectra are dominated by several Raman lines, denoted by asterisks. The atomic displacements of the phonons giving rise to these lines, are shown in Figs. 5–7 for the MV, DV, and SW cases, respectively.

For the MV structure, the phonons, giving rise to high intensity lines, are with predominant out-of-plane displacement ($282, 305, \text{ and } 489 \text{ cm}^{-1}$; see Fig. 5, the out-of-plane displacements are not shown) but there is also an intense phonon with predominant in-plane displacements at

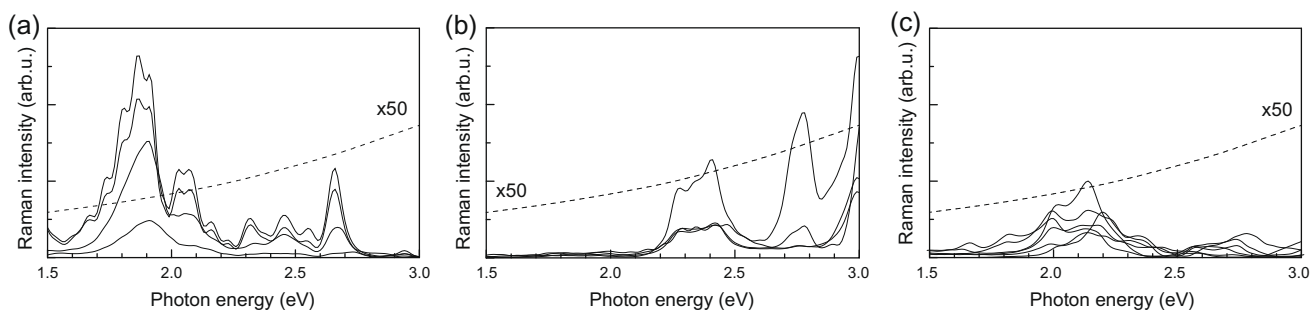


Fig. 3 – The resonance excitation profiles of phonons of graphene with three different point defects: (a) MV, (b) DV, and (c) SW. Only the profiles with most intense peaks are presented. These profiles give rise to intense lines, denoted by asterisks in the Raman spectra in Fig. 4, and belong to phonons, shown in Figs. 5–7. The profile of the G-mode in perfect graphene is also provided for comparison (dashed line, scaled $\times 50$).

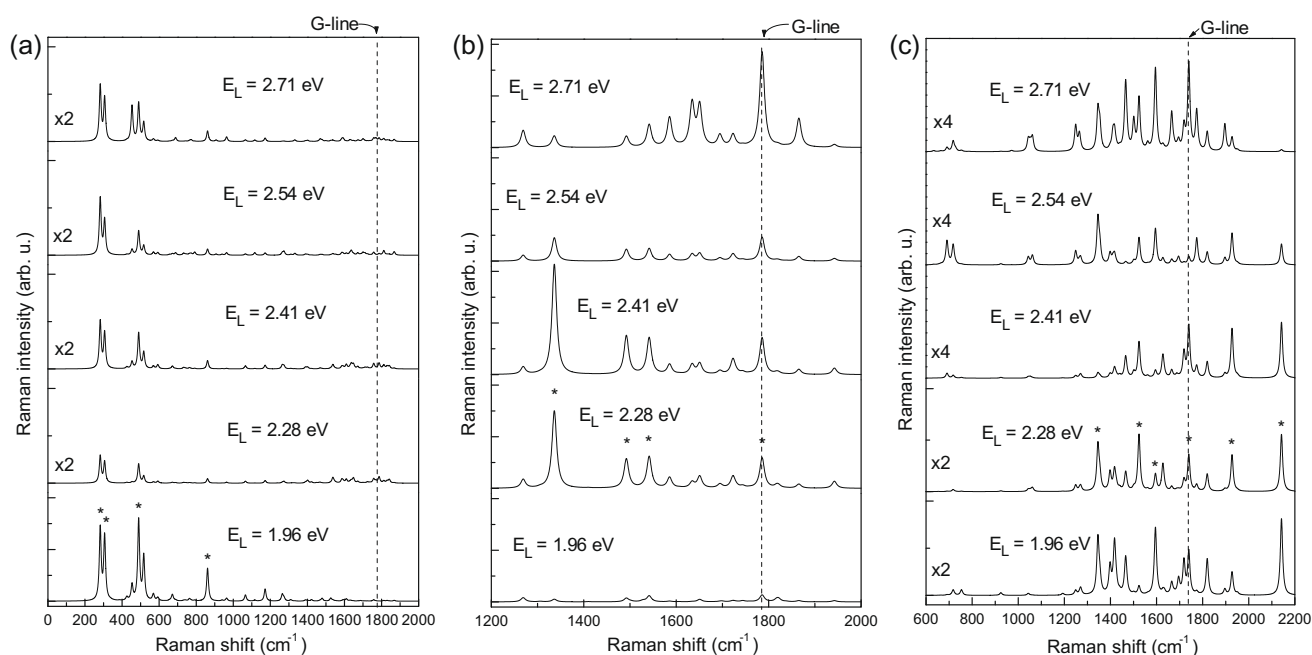


Fig. 4 – The Raman spectra of graphene with different point defects for five laser photon energies E_L : (a) MV, (b) DV, and (c) SW. Only the frequency region with more prominent Raman features is shown. Some of the spectra are scaled for better presentation. The most intense Raman lines are denoted by asterisks and are discussed in the text.

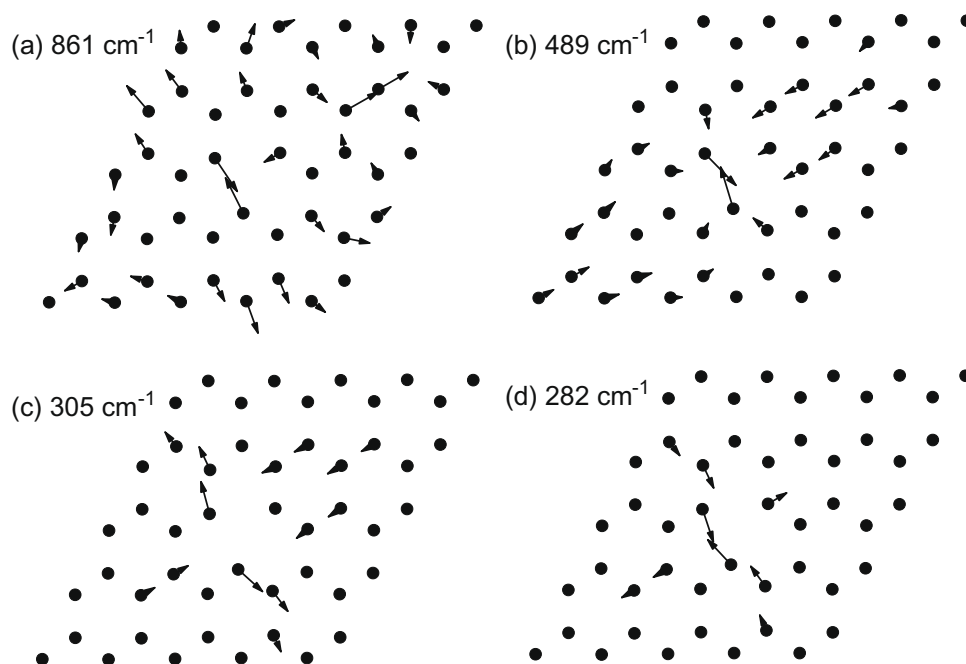


Fig. 5 – Atomic displacements for four phonons (a–d) of the MV structure with most intense Raman lines. The numbers are the phonon frequencies.

861 cm^{-1} . In the latter, the three atoms, as well as two hexagons adjacent to the vacancy, have a breathing-like motion. There is also a G-mode-like phonon giving rise to a low-intensity line at 1787 cm^{-1} .

The situation with the DV and SW structures is quite different. These structures are almost flat and the out-of-plane

phonons have negligible intensity. In the DV case, there are four phonons with intense lines (1336 , 1492 , 1542 , and 1786 cm^{-1} ; see Fig. 6). For all of them, the displacement of the atoms close to the two vacancies are small compared to that of other atoms with the exception of the phonon at 1542 cm^{-1} . Nevertheless, all these phonons can be called "de-

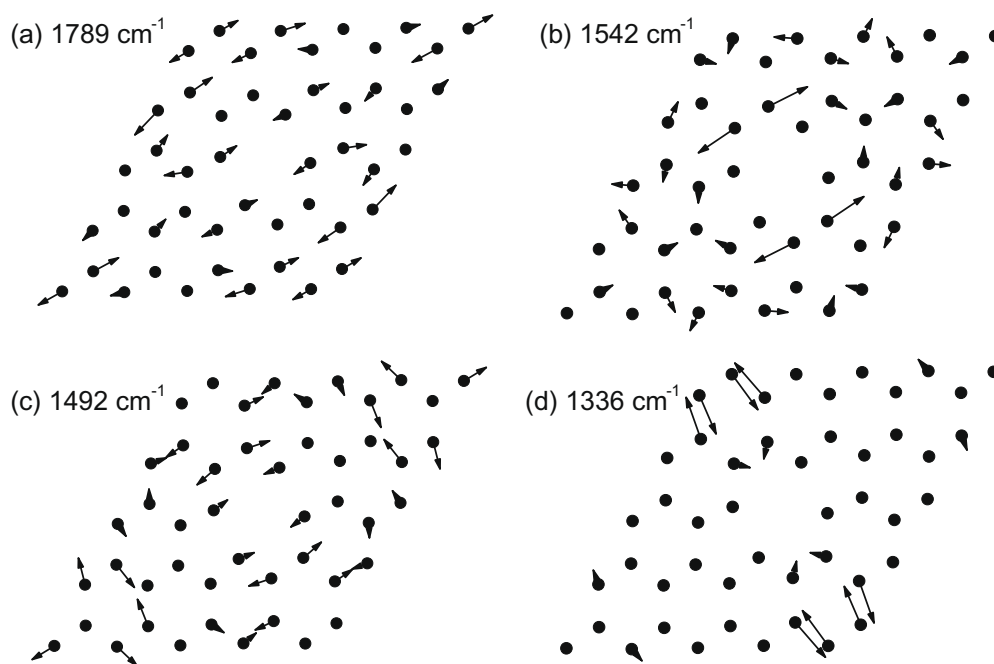


Fig. 6 – Atomic displacements for four phonons (a–d) of the DV structure with most intense Raman lines. The numbers are the phonon frequencies.

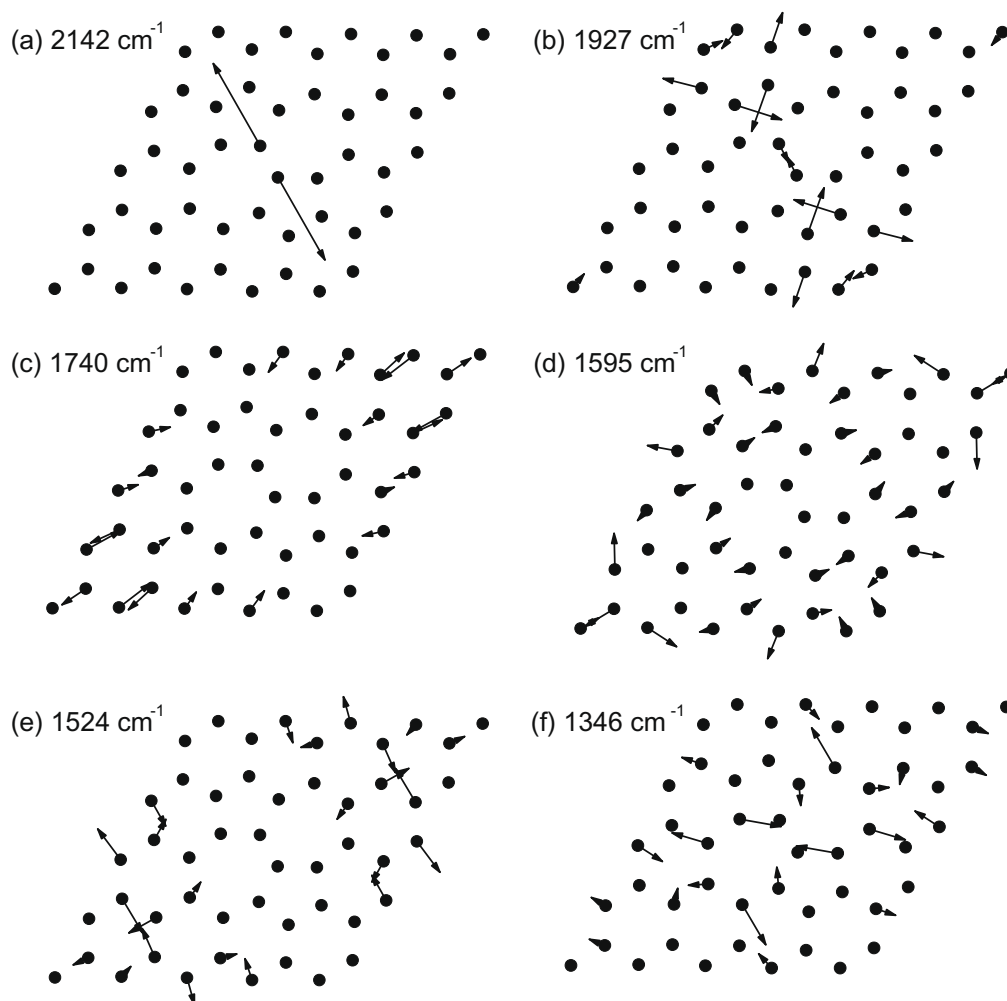


Fig. 7 – Atomic displacements for six phonons (a–f) of the SW structure with most intense Raman lines. The numbers are the phonon frequencies.

fect” ones in a sense that they appear because of defect-induced deformation of perfect graphene and, therefore, may serve as signatures of the DV structure. Among the intense lines there is a line at 1786 cm^{-1} , which is due to a G-mode-like phonon. As in the MV case, this phonon is obtained with almost the same frequency as the G-mode of perfect graphene. Therefore, the defect-induced deformations of the graphene lattice practically do not change the frequency of this phonon.

For the SW structure, the calculations yield six intense lines (1346 , 1524 , 1595 , 1740 , 1927 , and 2142 cm^{-1} ; see Fig. 7). As for the DV case, the SW structure is almost flat and the phonons, giving rise to these lines, are with predominant in-plane displacements. The four lowest-frequency phonons involve motion of the atoms of the heptagons, while the two highest-frequency ones are displacements of the atoms of the pentagons. The phonon at 1740 cm^{-1} is a red-shifted modification of the G-mode. Out of the various defect phonons, the one at 2142 cm^{-1} is well-separated and has high intensity, and can be taken as a specific spectroscopic signature of the SW defect. This value overestimates the *ab initio* one of 1820 cm^{-1} (Ref. [17]) by 17.7%, which is in accord with the overestimation of the frequency of the bond-stretching modes within the tight-binding model. The larger factor can be attributed to the stronger bonding of the carbon atoms in the pentagons. It is seen from the displacement pattern of the defect phonons of all three structures that only the latter phonon is strongly localized at the point defect. More precise conclusions about the degree of localization of phonons can be drawn from a future study using larger supercells.

Finally, the effect of the presence of defects on the G-mode intensity can be illustrated by comparison of the calculated values with those for perfect graphene and available experimental Raman data [27]. In Fig. 8, the intensity of the G-mode-like phonons of the MV, DV, and SW structures relative to that of the G-mode in perfect graphene is shown. It is seen that, for photon energies between 1.9 and 2.7 eV, the relative

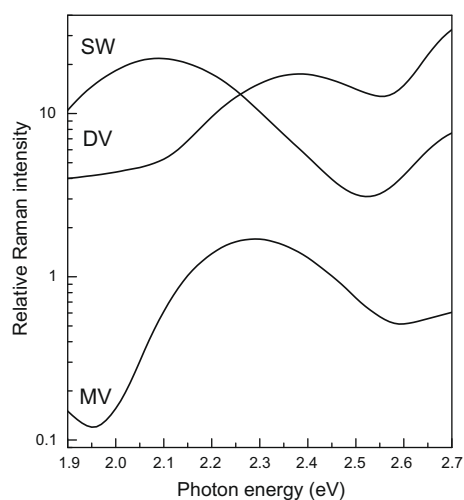


Fig. 8 – Relative Raman intensity of the G-mode-like phonons in the MV, DV, and SW structures with respect to that of the G-mode in perfect graphene.

intensity varies roughly in the ranges (0.1,1.1), (4,30), and (3,20) for the MV, DV, and SW cases, respectively. Therefore, the DV and SW defects modify the electronic structure leading to generally higher Raman intensity of the G-mode. In the considered case of large defect density (one defect per 25 unit cells of perfect graphene), the spectra of structures with defects can be dominated by other much more intense Raman lines, originating from defect phonon modes. However, most of these lines lie in the frequency range of the broad D-band, which could make their observation difficult.

In the photon energy range from 1.9 to 2.7 eV, the relative intensity of the G-mode in perfect graphene with respect to available Raman data on HOPG [27] decreases by an order of magnitude. This trend is generally seen for the three defect structures as well, the decrease being smallest for the DV case. Thus, the experimental excitation profile exhibits faster increase with the increase of the photon energy than predicted for any of the four cases considered here. It is possible that this behaviour of the experimental profile could be explained by a combination of different defects or other processes beyond the simple one-phonon scattering.

4. Conclusions

We calculated within a tight-binding model the optimized structure, phonons, and Raman intensity of graphene with three different types of point defects: a mono-vacancy, a di-vacancy, and a Stone–Wales defect. The results for the phonons and the intensity allow us to determine spectroscopic signatures of these defects. In particular, an isolated Stone–Wales defect has a well-separated defect-induced phonon with frequency of 2142 cm^{-1} . This frequency, when reduced by $\approx 18\%$, agrees with other estimations and can be used for identification of this defect. In addition to other similar theoretical studies of graphene with defects, we show that the presence of defects leads to modifications of the electronic structure and the optical transitions. For all the three defect structures, optical transitions appear in the visible range, when 5×5 supercells are used. This results in a resonant enhancement of the Raman scattering from defect-induced phonons and G-mode-like phonons for certain photon energies in this range.

The obtained predictions for the Raman spectra of graphene with defects can be used in the analysis of experimental Raman data. They can be applied for estimation of the density of the three types of defects in the samples, assuming linear increase of the intensity with the increase of the defect density. At present, there are no reports of Raman observation of defect phonons, possibly, because of the masking of their lines by the D-band and the lack of predicted signatures.

Acknowledgements

V.N.P. was supported partly by the Marie-Curie European Reintegration Grant MERG-CT-2007-201227 within the 7th European Community Framework Programme. L.H. was supported by the FRS-FNRS and in part by the European Commission under the 6th Framework Programme (STREP project BNC Tubes, contract number NMP4-CT-2006-03350). V.N.P., L.H., and Ph.L.

acknowledge the support by the NATO Collaborative Linkage Grant CBP.EAP.CLG.982722.

 REFERENCES

- [1] Novoselov KS, Geim AK, Morozov SV, Jiang D, Zhang Z, Dubonos SV, et al. Electric field effect in atomically thin carbon films. *Science* 2004;306(5696):666–9.
- [2] Charlier JC, Eklund PC, Zhu J, Ferrari AC. Electron and phonon properties of graphene: their relationship with carbon nanotubes. In: Jorio A, Dresselhaus G, Dresselhaus MS, editors. *Topics of Applied Physics*, vol. 111. Berlin: Springer; 2008. p. 673–709.
- [3] Kushmerick JG, Kelly KF, Rust HP, Halas NJ, Weiss PS. Observations of anisotropic electron scattering on graphite with a low-temperature scanning tunneling microscope. *J Chem Phys* 1999;103(10):1619–22.
- [4] Hahn JR, Kang H. Vacancy and interstitial defects at graphite surfaces: scanning tunneling microscopic study of the structure, electronic property, and yield for ion-induced defect creation. *Phys Rev B* 1999;60(8):6007–17.
- [5] Hashimoto A, Suenaga K, Gloter A, Urita K, Iijima S. Direct evidence for atomic defects in graphene layers. *Nature* 2004;430(7002):870–3.
- [6] Thrower PA. In: Walker Jr PL, editor. *Chemistry and physics of carbon*, vol. 5. New York: Dekker; 1969. p. 262.
- [7] Stone AJ, Wales DJ. Theoretical studies of icosahedral C₆₀ and some related species. *Chem Phys Lett* 1986;128(5–6):501–3.
- [8] Yoon M, Han S, Kim G, Lee S, Berber S, Osawa E, et al. Zipper mechanism of nanotube fusion: theory and experiment. *Phys Rev Lett* 2004;92(7):075504-1–4.
- [9] Kelly KF, Sarkar D, Hale GD, Oldenburg SJ, Halas NJ. Threefold electron scattering on graphite observed with C₆₀-adsorbed STM tips. *Science* 1996;273(5280):1371–3.
- [10] Vitali L, Schneider MA, Kern K, Wirtz L, Rubio A. Phonon and plasmon excitation in inelastic electron tunneling spectroscopy of graphite. *Phys Rev B* 2004;69(12):121414-1–121414-12.
- [11] Amara H, Latil S, Meunier V, Lambin Ph, Charlier JC. Scanning tunneling microscopy fingerprints of point defects in graphene: a theoretical prediction. *Phys Rev B* 2007;76(11):115423-1–115423-10.
- [12] Ferrari AC, Robertson J. Interpretation of Raman spectra of disordered and amorphous carbon. *Phys Rev B* 2000;61(20):14095–107.
- [13] Ferrari AC, Robertson J. Resonant Raman spectroscopy of disordered, amorphous, and diamond like carbon. *Phys Rev B* 2001;64:075414-1–075414-13.
- [14] Reich S, Thomsen C. Raman spectroscopy of graphite. *Philos Trans R Soc London A* 2004;362(1824):2271–88.
- [15] Ferrari AC, Meyer JC, Scardaci V, Casiraghi C, Lazzeri M, Mauri F, et al. Raman spectrum of graphene and graphene layers. *Phys Rev Lett* 2006;97:187401-1–4.
- [16] Casiraghi C, Pisana S, Novoselov KS, Geim AK, Ferrari AC. Raman fingerprint of charged impurities in graphene. *Appl Phys Lett* 2007;91:233108-1–3.
- [17] Wu G, Dong J. Raman characteristic peaks induced by the topological defects of carbon nanotube intramolecular junctions. *Phys Rev B* 2006;73(24):245414-1–9.
- [18] Kudin KN, Ozbas B, Schniepp HC, Prudhomme RK, Aksay IA. Raman spectra of graphite oxide and functionalized graphene sheets. *Nano Lett* 2008;8(1):36–41.
- [19] Porezag D, Frauenheim Th, Köhler Th. Construction of tight-binding-like potentials on the basis of density-functional theory: application to carbon. *Phys Rev B* 1995;51(19):12947–57.
- [20] Popov VN, Henrard L. Comparative study of the optical properties of single-walled carbon nanotubes within orthogonal and nonorthogonal tight-binding models. *Phys Rev B* 2004;70(11):115407-1–115407-12.
- [21] Popov VN, Lambin Ph. Radius and chirality dependence of the radial breathing mode and the G-band phonon modes of single-walled carbon nanotubes. *Phys Rev B* 2006;73(8):085407-1–9.
- [22] Martin RM, Falicov L. In: Cardona M, editor. *Light scattering in solids*, topics of applied physics, vol. 8. Berlin: Springer; 1975. p. 80–148.
- [23] Popov VN, Henrard L, Lambin Ph. Electron–phonon and electron–photon interactions and resonant Raman scattering from the radial-breathing mode of single-walled carbon nanotubes. *Phys Rev B* 2005;72(3):035436-1–035436-10.
- [24] Piscanec S, Lazzeri M, Mauri F, Ferrari AC, Robertson J. Kohn anomalies and electron–phonon interactions in graphite. *Phys Rev Lett* 2004;93(18):185503-1–7.
- [25] El-Barbary AA, Telling RH, Ewels CP, Heggie MI, Briddon PR. Structure and energetics of the vacancy in graphite. *Phys Rev B* 2003;68(14):144107-1–7.
- [26] Lehtinen PO, Foster AS, Ma Y, Krashennikov AV, Nieminen RM. Irradiation-induced magnetism in graphite: a density functional study. *Phys Rev Lett* 2004;93(18):187202-1–4.
- [27] Sinha K, Menéndez J. First- and second-order resonant Raman scattering in graphite. *Phys Rev B* 1990;41(15):10845–7.